FULL-WAVEFORM LIDAR RECOVERY AT SUB-NYQUIST RATES

Juan Castorena and Charles D. Creusere
Advising Professor: Dr. Charles D. Creusere
Department of Electrical and Computer Engineering
New Mexico State University
Las Cruces, NM, 88003, USA

Abstract

Third generation LIDAR full-waveform (FW) based systems collect 1D FW signals of the echoes generated by laser pulses of wide bandwidth reflected at the intercepted objects to construct depth profiles along each pulse path. By emitting a series of pulses towards a scene using a predefined scanning pattern, a 3D image containing spatial-depth information can be constructed. Unfortunately, acquisition of a high number of wide bandwidth pulses is necessary to achieve high depth and spatial resolutions of the scene. This implies the collection of massive amounts of data which generate problems for the storage, processing and transmission of the FW signal set. In this research, we explore the recovery of individual continuous-time FW signals at sub-Nyquist rates. The key step to achieve this is to exploit the sparsity in FW signals. Doing this allows one to sub-sample and recover FW signals at rates much lower than that implied by Shannon's theorem. Here, we describe the theoretical framework supporting recovery and present the reader with examples using real LIDAR data.

Keywords: LIDAR, full-waveform, sub-Nyquist sampling, overlapping windows.

1 Introduction

Light detection and ranging (LIDAR) is a primary tool that provides excellent capabilities for acquiring 3D images of a scene. The most popular systems to date operate under the time-of-flight (TOF) principle of the laser pulse to determine object depth. Among these kind, third generation pulsed LIDAR systems collecting full-waveform (FW) signals consisting of the pulse echoes have gained popularity in the last few years. Their popularity has increased because of the improved object depth estimation and scene structure characterization capabilities [11] (e.g, inclination, smoothness, vegetation, urban area).

In general, these systems project an energy pulse from a single laser source into a scene and measure the echoes generating from the pulse interaction with the objects encountered. Each of these echoes is sensed with a single photodetector or avalanche photodiode and

sampled using an A/D converter. Measurements of such signals provide depth information of the objects intercepted by the pulse along a specified direction. An illustration of this process for a single transmitted pulse is best described with aid of Figure 1.

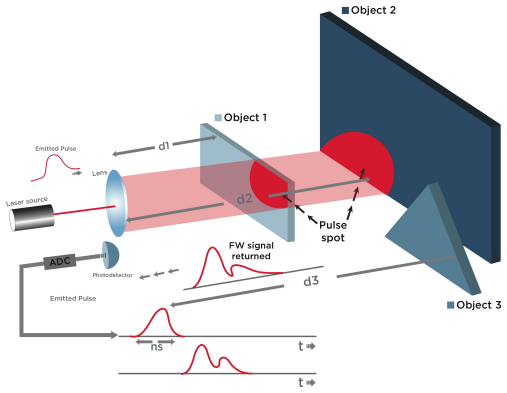

Figure 1: A pulse encounters two objects at distinct depths which create pulse echoes received at the photodetector. The shape and time of flight (TOF) of these echoes depend on the object characteristics and on the distance from the emitter to the encountered object.

By emitting a series of pulses and directing them with a mechanical scanning unit into distinct locations through the entire scene of interest and measuring the corresponding echoes, connected FW signals of 3D scenes can be readily obtained. This set of FW signals can be used to construct 3D images of the scene after the appropriate processing. Unfortunately, a high density of pulse emissions and the corresponding acquisitions is required to achieve acceptable spatial resolutions of the scene. For example, a typical scene is scanned by emitting hundreds of millions of pulses and collecting the corresponding FW signals [14]. Moreover, each LIDAR pulse is of short duration and of wide bandwidth which implies sampling at high rates (e.g., sampling at a few Gigahertz (GHz)) if sampled under the Shannon/Nyquist principle [15], [13]. Sampling such FW signal sets of a scene is thus an extremely expensive task because of the massive amounts of data collected.

Fortunately, the set of FW signals collected at Nyquist rates contains many redundancies. From one point, the multiple pulse echoes occupy only a very small portion of the measurement time interval of the individual FW signals (we refer to echoes with this feature as echoes of short-time duration). This in turn, implies that the set of FW signals is highly sparse and that the system is sampling at unnecessarily high rates. We can, thus, take advantage of this structure to devise sub-sampling procedures that sample more efficiently.

In [8], [9] the authors developed a TOF based pulsed laser system that can sample a scene very efficiently using a spatial light modulator. Such approach follows the same principle as the single-pixel camera developed in [6] for 2D images. The strategy produces good quality depth images using just a few samples compared to what traditional Nyquist theorem dictates. However, the sampling process stores only the TOF of the pulse (i.e., a single TOF number per pulse emission) and not the FW signal. Different to these approaches, we are interested on devising sub-Nyquist sampling strategies that can recover the FW signal set for subsequent scene analysis. In [4], the authors model FW signals as signals with finite rate of innovations. This allows to sub-sample individual FW signals at the rate of innovation; a

number which describes the number of parameters representing the FW signal. The authors found that under this strategy the size of the collected FW signal set can be significantly reduced and still achieve high quality reconstructions. Here, we devise sub-Nyquist strategies for individual FW signals by sampling using overlapping random windows instead.

2 LIDAR Dataset Characteristics

2.1 Individual FW signal characteristics

To begin, we introduce the term echo which is referred to in here as the pulse reflection caused by a single object regardless of its characteristics. In general, a FW signal might consist of multiple short-duration echoes generated by the presence of multiple objects encountered during the time of flight (TOF) of the pulse. The shape of each of the echoes varies according to the particular characteristics of the objects encountered (e.g., object depth, inclination, roughness, reflectivity) [10], [12], [11] and [16] and on the characteristics of the emitted pulse. For LIDAR, the emitted pulse is typically of short duration and in the range of a couple of nanoseconds (ns).

The spectrum of the FW signal is of wide bandwidth as described by the uncertainty principle [7] because the echoes are well localized temporally. Because the emitted pulse is of a few nanoseconds of duration then its spectrum is bandlimited to a few Gigahertz (GHz). It is also expected that the FW signal spectrum is similar to the spectrum of the emitted pulse. An illustration showing an example of the emitted pulse and the FW signal generated by the corresponding echoes is shown in Figure 2.

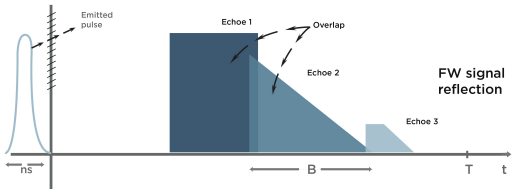

Figure 2: A full-waveform signal consisting of three echoes of distinct shape.

Here, we refer to the continuous-time FW signal as the signal $x(t)$ for $t \in [0, T]$ and with T finite. The interval $[0, T]$ contains all the salient information pertaining to the encountered objects in the TOF of the pulse. In particular, $t = 0$ corresponds in general to the time at which the laser pulse was emitted. The number T is selected according to the system characteristics; its capabilities to resolve far-field objects and the intended application. We assume no knowledge on the shape and TOF of the echo. The echoes in the FW signal might be overlapping with each other if two or more of the intercepted objects are relatively close as shown in Figure 2. Here, the term relatively close is measured with respect to the pulse duration. The sections of the FW signal corresponding to the pulse echoes are defined to in here as $\Gamma_e \subseteq [0, T]$ and its cardinality by $S_e = |\Gamma_e|$. Note that in the absence of noise S_e is equivalent to $S_e = S = |\operatorname{supp}(x(t))|$ (i.e., the support of the FW signal). In addition, S_e is much smaller than T (i.e., $S_e \ll T$) in general. We also refer to Γ_e^c as the subset in $[0, T]$ complement to Γ_e. Thus, the set Γ_e^c describes the indices in the FW signal which do not

correspond to echoes. We can further explore the components that make up S_e. If disjoint echoes, S_e is made up of the number of echoes N_e and on the duration d_i for $i \in (1, N_e)$ of each of these echoes, in other words, $S_e = \sum_{i=1}^{N_e} d_i$. Unfortunately, N_e and d_i are generally unknown prior to FW signal acquisition.

2.2 FW signal set

By scanning, we collect a set of FW signals which contains the spatial and temporal (i.e., depth) information of the 3D scene of interest. Here we refer to scanning, as the process of emitting pulses towards the scene locations following a pattern and measuring the corresponding FW signals. The set of FW signals is arranged as a 2D matrix where each row corresponds to a FW signal and columns index a specific time. The order in which FW signals is arranged in the 2D matrix depends on the order specified by the scanning pattern (i.e., the order in which pulses are emitted). The FW signal set typically contains many zeros because the multiple echoes are of short duration (i.e., sparse).

2.3 On real data

The LIDAR dataset obtained from NAVAIR China Lake, CA was collected using the VISSTA ELT LADAR system. The shot rate of this system is 20 Khz (i..e, pulse emission rate). Each time a pulse of 1.5 ns of duration at full width half maximum is transmitted, the echo return waveforms are captured at a sampling rate of 2 Ghz and quantized using an 8-bit A/D converter. The dataset used in this research was collected by imaging a pickup truck through a chain link fence both positioned perpendicular to the pulse transmission path. To illustrate this more clearly, Figure 3 shows the 3D point cloud resulting from processing the waveforms collected by the system. The raw FW signal set contains a total number of 31,626 pulse emissions and corresponding measurements, representing, a total of 126×251 pulses along the vertical and horizontal directions, respectively.

Figure 3: An example of the LIDAR point cloud

A representative example of a measured FW signal is shown in Figure 4a. Note that in general, the occupation of the echoes is much smaller than the signal length. In fact, most samples are noise and only a small portion of them contain the echo components. In addition, we include in Figure 4b a small section of the FW signal set. Each row represents a distinct FW signal and the columns represents a time index. The white entries represent noise and the darker regions indicate the time indices at which echoes are present. Note that in general, the FW signal set is very sparse.

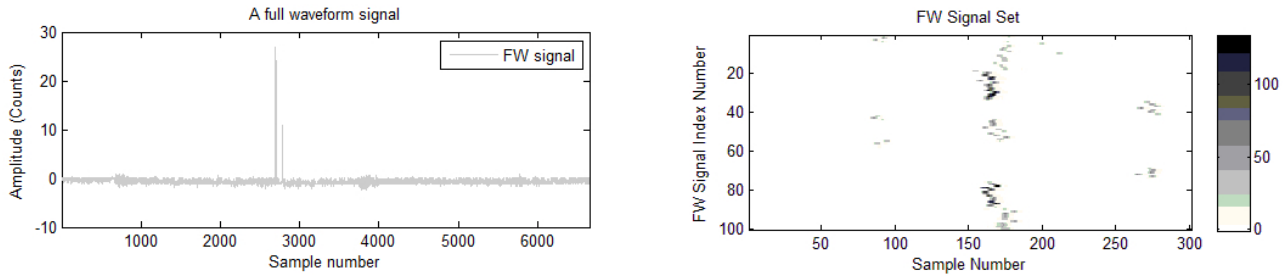

(a) Full-waveform signal (b) A section of the set of FW signals

Figure 4: Examples of the FW LIDAR data.

3 Sub-sampling of individual FW signals

3.1 Sub-sampling Approach

As described in section 2.1, echoes in individual FW signals occupy a small portion of T. As such, we devise a sampling approach which can take advantage of such structure. The approach we follow is similar in nature to the short-time Fourier transform in which Fourier transforms are obtained from sections of the signal dictated by overlapping windows. Here however, the elements of the overlapping window are of random nature and of fixed length T_b and shift T_s. In general, sub-samples of the signal sections are collected by the appropriate multiplication of the overlapping window with the signal $x(t)$ followed by integration and sampling. The general implementation consists of the bank of samplers illustrated in Figure 5. The overlapping windows denoted by $\Phi_{(j)}(t)$ for $j \in (1, q)$ where q represents the number

$$
\begin{array}{lll}
 & x(t)\Phi_{(1)}(t) & \\
x(t) \rightarrow & \otimes \longrightarrow & \boxed{\int_{t_1}^{t_1+T_b} x(t)\Phi_{(1)}(t)dt} \rightarrow \boxed{\text{S/H}} \rightarrow y_1[1] \\
 & \uparrow & \\
 & \Phi_{(1)}(t) & \\
 & x(t)\Phi_{(2)}(t) & \\
x(t) \rightarrow & \otimes \longrightarrow & \boxed{\int_{t_2}^{t_2+T_b} x(t)\Phi_{(2)}(t)dt} \rightarrow \boxed{\text{S/H}} \rightarrow y_2[1] \\
 & \uparrow & \\
 & \Phi_{(2)}(t) & \\
 & \vdots \quad\quad\quad \vdots \quad\quad\quad \vdots & \\
 & x(t)\Phi_{(q)}(t) & \\
x(t) \rightarrow & \otimes \longrightarrow & \boxed{\int_{t_q}^{t_q+T_b} x(t)\Phi_{(q)}(t)dt} \rightarrow \boxed{\text{S/H}} \rightarrow y_q[\lceil \tfrac{M}{q} \rceil] \\
 & \uparrow & \\
 & \Phi_{(q)}(t) &
\end{array}
$$

Figure 5: Parallel implementation of random demodulators

of channels in the system, changes its value at rate $f_N = 1/T_N$. In other words,

$$\Phi_j(t) = \Phi_{j,n}, \text{ for } t \in (j-1)T_s \cdot \mathcal{B}_n \tag{1}$$

for $n = 1, ..., N$, $N = T/T_N$, set $\mathcal{B}_n = [(n-1)T_N, n \cdot T_N)$ and $\Phi_{j,n}$ is a sub-Gaussian random variable (r.v.). An alternative representation in terms of the rect function is given by

$$\widetilde{\Phi}_m(t) = \Phi_j(t) \cdot \text{rect}(\frac{t}{T_b} - (i-1)T_b - (j-1)T_s) \tag{2}$$

where $m = q(i-1) + j$ for $m \in [1, M], i \in [1, \lceil M/q \rceil], j \in [1, q]$. We can rewrite (2) as

$$\begin{aligned} \widetilde{\Phi}_m(t) &= \widetilde{\Phi}_{m,n} \text{ for } t \in \mathcal{B}_n \\ &= \begin{cases} \Phi_{m,n} & \text{for } t \in \mathcal{A}_m \cap \mathcal{B}_n \\ 0 & \text{otherwise} \end{cases} \end{aligned} \tag{3}$$

for $m = 1, .., M$, $n = 1, ..., N$, set $\mathcal{A}_m = [(m-1)T_s, (m-1)T_s + T_b)$ and where $\Phi_{m,n}$ denotes a sub-Gaussian r.v. Note that although the random waveforms $\widetilde{\Phi}_m(t)$ are continuous, these, can be represented by a finite number of variables when the waveforms are considered over a finite extent $N \cdot T_N$. This representation allows us to model the system by

$$y[m] = \sum_{n=1}^{N} \widetilde{\Phi}_{m,n} x[n] \text{ or } y = \widetilde{\Phi} x \text{ where } x[n] = \int_{(n-1)T_N}^{nT_N} x(t)dt. \tag{4}$$

Here, $\widetilde{\Phi} \in \mathbb{R}^{M \times N}$ denotes the measurement matrix with banded random matrix (BRM) structure and $x \in \mathbb{R}^N$ is a vector containing signal averages over intervals of length T_N.

3.2 FW signal recovery

The system model in (4) is an underdetermined system of equations because in general $\widetilde{\Phi}$ is rectangular with $M \ll N$. Fortunately, the theory of compressive sensing [3] asserts that the signal x can be recovered exactly from the measurements y if $\widetilde{\Phi}$ obeys the restricted isometry property (RIP) [2]. The optimization program to recover x is given by

$$\min \|\tilde{x}\|_1 \text{ subject to } \|\widetilde{\Phi}\tilde{x} - y\|_2 \leq \epsilon \tag{5}$$

where $\epsilon \geq 0$ is a small constant and the operator $\|\|_p$ denotes the l_p norm. In [] the authors determined that the number of measurements required such that $\widetilde{\Phi}$ satisfies the RIP with probability at least $1 - 2\exp(-c_0 b_v^2 \delta^2/\beta)$ for $c_0 > 0$ is given by

$$M \geq \lceil C[\log(N/S) + 1] + N/b_s - \Lambda(C_1, b_s, N, S) \rceil - 1. \tag{6}$$

For $S = S_e, b_s = T_s/T_N \in \mathbb{Z}, b_h = T_b/T_N \in \mathbb{Z}, b_v = b_h/b_s \in \mathbb{Z}$, . Here, the constant $C > 0$ with $C_1 = 2C$ is small and dependent on an error term $\delta \in (0, 1)$, on the sub-Gaussian norm K^2 of its entries, and on c_0, S stands for the sparsity or support of the signal. Furthermore, $\beta = (-2S^2 - (6b_v b_s + 3b_s + 1)S + b_s^2 - 1)/(6b_s S)$ and $\Lambda(C_1, b_s, N, S) = (-3C_1 b_s \log(eN/S)[4S^2 - (3C_1 b_s \log(eN/S) + 2(3b_s + 1))S + 2(b_s^2 - 1)])^{(1/2)}/(6b_s\sqrt{S})$.

3.3 Implementation

The implementation of the system is performed by replacing the ADC in Figure 1 by the system consisting of the bank of random samplers shown in Figure 5 sampling at sub-Nyquist rates. To sample FW signals we use the approach described in section 3.1 and the model in (4). The rate f_N is a very important factor in the design of the sampling approach and should be chosen carefully. Note in (4) that the faster the rate, the higher the resolution of the reconstruction that can be achieved and vice versa. In the case when a reconstruction of the type of quality given by the Nyquist/Shannon sampling theorem is desired, the rate f_N, has to be conditioned to be equal or higher the Nyquist rate f_{Nyq} (i.e., $f_N \geq f_{Nyq}$ where $f_{Nyq} \geq 2f_{max}$ and where f_{max} is the highest frequency present in the spectrum of $x(t)$). Selecting such a rate gives the capability to achieve a reconstruction as the one given by the Shannon/Nyquist theorem but with fewer measurements under sparsity assumptions. Therefore, the desirable resolution depends on the application: whether a single TOF measurement is sufficient or a FW signal for subsequent analysis is desired.

One of the parameters determining the number of measurements required depends as described in (6) on $S = S_e$. However, in section 2.1 it was mentioned that the number of echoes N_e and their duration d_i is generally unknown. Therefore, we require some sort of estimation on the parameter S_e to sample the signal very efficiently. In [5] the authors defined the term complexity of the signal as a parameter representing the number of innovations of the signal. Such number, can be used as an indicator of the sparsity of the signal and updated on the fly as the set of sampled FW signals are collected by the process of scanning. In general, this is possible because S_e does not vary largely with FW signal index as shown in Figure 4b. Unfortunately, this information is not available initially. However, the initial values of S_e can be chosen with knowledge of the emitted pulse duration and on the maximum number of echoes typically present in FW signals. For example [12] determined empirically that the maximum number of echoes present in FW signals is in general seven (i.e., $N_e = 7$) and that more than four echoes occur quite rarely. It is also mentioned here that the first two echoes contain about 90% of the emitted pulse energy.

4 Experimentation and Results

To perform the experimentation, we use the collected dataset described in section 2.3. Simulation of the sub-sampling approach and recovery described in section 3 is performed in Matlab. The recovery of FW signals using the optimization in (5) is made by using the code developed in [1]. To illustrate the possibilities of our approach, we use several real LIDAR FW signals as input to the system depicted in Figure 5. The rate at which these signals were originally sampled is 2 GHz. This rate is selected based on the characteristics of the emitted pulse of 1.5 ns duration and the corresponding Nyquist rate.

In the first set of experiments, the selected rates f_N of the overlapping windows $\Phi_j(t)$ are $f_N \in \{1/4f_{Nyq}, 1/3f_{Nyq}, 1/2f_{Nyq}, f_{Nyq}\}$. At each of these selected rates, recovery is performed using a specific number of samples. The overlapping windows are simulated via the observation matrix $\widetilde{\Phi}$ with a BRM structure. The non-zero entries in the BRM are randomly generated in Matlab according to a Normal distribution. The duration of the

Table 1: FW signal recovery with parameter f_N

	f_N	M	N	b_h	CR (%)
Resolution 1	$1/4f_{Nyq}$	1054	1665	790	36.7
Resolution 2	$1/3f_{Nyq}$	1239	2220	896	44.2
Resolution 3	$1/2f_{Nyq}$	1608	3327	1035	51.7
Resolution 4	f_{Nyq}	2718	6657	1500	59.2

overlapping windows is fixed to $b_h = \{790, 896, 1035, 1500\} \cdot 1/2e9$ seconds for the rates $f_N \in \{1/4f_{Nyq}, 1/3f_{Nyq}, 1/2f_{Nyq}, f_{Nyq}\}$, respectively. At each of these cases the shift is fixed to $b_s = 3 \cdot 1/2e9$ which corresponds to a $b_v = 500 \cdot 1/2e9$ throughout all cases. Figures 6.1a, 2a show the random sub-samples, Figures 6.1b, 2b compare the original FW signal with the reconstructed signal and Figures 6.1c,2c is a zoomed version at the pulse echoes.

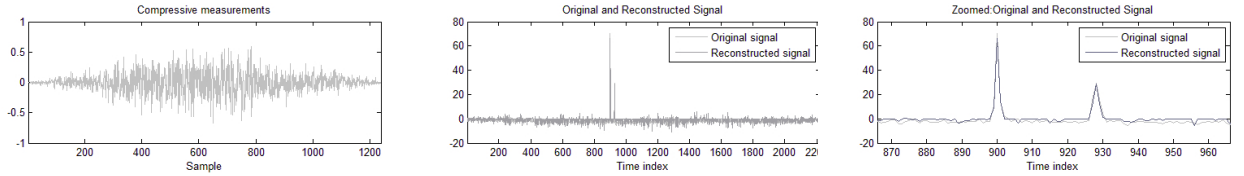

(1a) Measurements (1b) Original and reconctruction (1c) Zoomed echoes

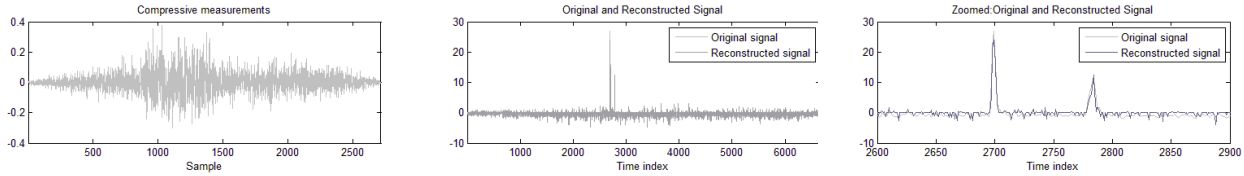

(2a) Measurements (2b) Original and reconctruction (2c) Zoomed echoes

Figure 6: Effect of the resolution parameter f_N. Figures 6.1a-c and 6.2a-c represent the measurements and FW signals obtained at rates $1/3f_{Nyq}, f_{Nyq}$, respectively.

Note that the the perceptual quality of the reconstructed signal is very close to that of the original signal using fewer samples as compared to the Nyquist/Shannon sampling theorem. To further asses the performance of our approach we measure the compression efficiency by means of the compression ratio (CR) given by $CR = (1 - \frac{M}{N}) \cdot 100\%$ where M and N denote the number of compressive samples and the number of Nyquist samples, respectively. Table 1 summarizes the results of for the distinct f_N cases in this experiment.

In addition to the experiment above, we also test our approach in reconstructing the FW signal as a function of the number of measurements M at a fixed rate f_N. In particular, we chose the rate $f_N = f_{Nyq}$ and reconstruct at distinct number of measurements M. The cardinality S_e of the echoes in the FW signal shown in Figure 6.1b is approximately about 29 samples which corresponds to 14.5 ns. In general the noise level in FW signals is large in the set Γ_e^c. With such noise, precise recovery would require a larger number of measurements M. To illustrate on how large noise increases the requirements on M, we compare, the performance of our sampling approach in the noisy and noiseless FW signal. In the noiseless scenario, we remove noise by modeling the FW signa as linear splines as done in [4]. The

Table 2: FW signal recovery with varying M

M	b_h	b_v	b_s	RMSE Noisy	RMSE Noiseless	CR (%)
500	350	25	14	0.1791	0.1031	92.5
1000	1344	168	8	0.1352	1.38e-5	85.0
1500	845	169	5	0.1189	6.97e-6	77.5
2000	1344	336	4	0.1121	6.96e-6	70.0
2500	843	281	3	0.0980	8.89e-6	62.4

noisy and noiseless recovery results are shown in Figure 7.1 and 7.2, respectively. In the noisy setting the parameters $b_h = 845, b_v = 169, b_s = 5, M = 1500$ where used, whereas, $b_h = 1344, b_v = 168, b_s = 8, M = 1000$ where used in the noiseless case. The performance of the algorithm is measured by using the root mean squared error (RMSE). However, for convenience and relevance the RMSE is measured only in the indices present in the set Γ_e. In table 2, a summary of a variety of reconstructions with distinct test parameters is shown. For these tests, the FW signal shown in Figure 6.1b originally sampled with $N = 6657$ samples and with an overlapping window rate of $f_N = f_{Nyq}$ is used.

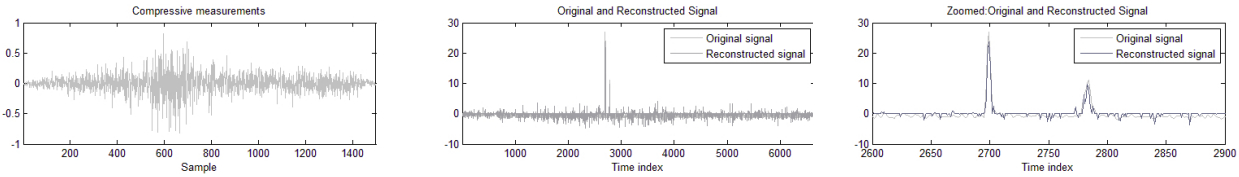

(2a) Measurements (2b) Original and reconctruction (2c) Zoomed echoes

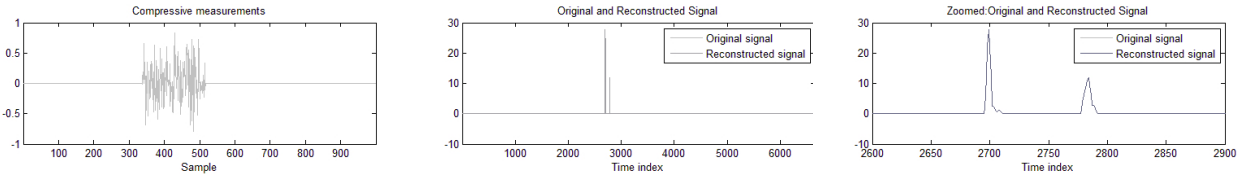

(4a) Measurements (4b) Original and reconctruction (4c) Zoomed echoes

Figure 7: Effect of M on FW signal recovery. Figures 7.1a-c, 7.2a-c, correspond to the noisy and noiseless setting with $M = 1000$ and $M = 1500$, respectively.

Note that the approach recovers the FW signal components corresponding to the echoes accurately. In contrast, the parts pertaining to the noise in the signal are unprecise because those sections are not sparse. Because these parts are irrelevant to the analyst and the noise peaks are kept to a minimum which prevents them from considered as a false echo then; we can say that the recovery is acceptable. However, careful selection of M is required to achieve acceptable recovery at a given noise level. Alternatively, we could also include a continuous-time noise reduction filter prior to signal digitization.

One other issue our approach presents is that the computational complexity is significantly high. We can expect improvements upon this issue by devising or using faster l_1 minimization algorithms. However, we leave that for future work and focus here on showing that FW signal recovery is possible using our proposed approach.

5 Conclusion

In the work presented here, we propose a framework to collect individual FW signals at sub-Nyquist rates. The essential key step to achieve recovery consists on exploiting the structure in multiple echoes which are of short duration. The sampling strategy consists on subdividing the FW signal using overlapping windows with random amplitudes. We model this process by banded random matrices (BRM) and recover using l_1 minimization under a restricted isometry property (RIP) condition. The experiments show that FW signals can be sampled and recovered very efficiently using our proposed method.

References

[1] E.J. Candes and J. Romberg. l1-magic.

[2] E.J. Candes and T. Tao. Decoding by linear programming. *IEEE Transactions on Information Theory*, 51(12):4203–4215, 2005.

[3] E.J. Candes and M.B. Wakin. An introduction to compressive sampling. *IEEE Signal Processing Magazine*, 25(2):21–30, March 2008.

[4] J. Castorena and C.D. Creusere. Compressive sampling of lidar: Full-waveforms as signals of finite rate of innovation. In *20th European Signal Processing Conference*, volume Accepted paper, Bucharest, Romania, August 2012.

[5] J. Castorena, C.D. Creusere, and D. Voelz. Using finite moment rate of innovation for lidar waveform complexity estimation. In *IEEE Conference Record of the Fourty Fourth Asilomar Conference on Signals, Systems and Computers (ASILOMAR)*, pages 608–612. IEEE, 2010.

[6] M.F. Duarte, M.A. Davenport, D. Takhar, J.N. Laska, T. Sun, K.F. Kelly, and R.G. Baraniuk. Single pixel imaging via compressive sampling. *IEEE Signal Processing Magazine*, 25(2):83–91, March 2008.

[7] D. Gabor. Theory of communication. *J. Inst. Elect. Eng. (London)*, 93(3)(26):429–457, 1946.

[8] G.A. Howland, P.B. Dixon, and J.C. Howell. Photon-counting compressive sensing laser radar for 3d imaging. *Applied Optics*, 50(31):5917–5920, November 2011.

[9] A. Kirmani, A. Colaco, F.N.C. Wong, and V. K. Goyal. Exploiting sparsity in time of flight range acquisition using a single time-resolved sensor. *Optics Express*, 19(22), October 2011.

[10] C. Mallet. *Full waveform topographic LIDAR*. PhD thesis, Telecom ParisTech, November 2010.

[11] C. Mallet, F. Bretar, M. Roux, U. Soergel, and C. Heipke. Relevance assessent of full-waveform lidar data for urban area classification. *ISPRS Journal of Photogrammetry and Remote Sensing*, 66:71–84, October 2011.

[12] C. Mallet, F. Lafarge, M. Roux, U. Soergel, F. Bretar, and C. Heipke. A marked point process for modeling lidar waveforms. *IEEE Transactions on Image Processing*, 19(12):3204–3221, December 2010.

[13] H. Nyquist. Certain topics in telegraph transmission theory. *Trans. Amer. Inst. Elect. Eng.*, 47:617–644, 1928.

[14] B. Schwarz. Lidar mapping the world in 3d. *Nature Photonics*, 4:429–431, July 2010.

[15] C.E. Shannon. Communication in the presence of noise. *Proc. IRE*, 37:10–21, 1949.

[16] Y. Sheng. Quantifying the size of a lidar footprint: A set of generalized equations. *IEEE Geoscience and Remote Sensing Letters*, 5(3):419–422, July 2008.